

Placement of a fast ion loss detector array for neutral beam injected particles in Wendelstein 7-X

D Kulla^{1,2,*} , S Lazerson¹ , S Günter³, M Hirsch¹, D Hartmann¹ , P McNeely¹, N Rust¹, R C Wolf¹  and the W7-X Team

¹ Max-Planck-Institut für Plasmaphysik Teilinstitut Greifswald, Wendelsteinstraße 1, DE 17491 Greifswald, Germany

² Technical University of Munich, Arcisstraße 21, München, DE 80333 Bayern, Germany

³ Max-Planck-Institut für Plasmaphysik, Boltzmannstraße 2, Garching bei München, DE 85748 Garching, Germany

E-mail: david.kulla@ipp.mpg.de

Received 18 October 2021, revised 2 December 2021

Accepted for publication 16 December 2021

Published 11 February 2022



CrossMark

Abstract

In light of measuring the fast ionized particle confinement in the stellarator Wendelstein 7-X, particles generated by the neutral beam injection system are simulated to determine the placement of an array of Faraday-cup fast ion loss detectors. This array is important due to the localization of the loss pattern, which changes drastically with experimental parameters. The Monte Carlo codes BEAMS3D and ASCOT5 are used for the simulations, following the particles from injection to wall collision. Different magnetic configurations and plasma pressures are investigated in this manner, and a configuration suitable for measuring the loss fraction is found. It qualitatively reproduces the global losses, is installable in locations of current carbon wall-tiles and the individual detector output appears well-suited for experimental purposes.

Keywords: fast ion, neutral beam, Wendelstein 7-X, stellarator, simulation, diagnostic

(Some figures may appear in colour only in the online journal)

1. Introduction and theory

1.1. Motivation

For a future fusion reactor, it will be imperative that the fast α -particles generated by the fusion of deuterium and tritium are well confined within the plasma. These particles are needed to sustain the fusion reaction, giving off their energy to the thermal plasma. However, if unconfined, they can also damage

the first wall, as they generate locally high heat fluxes. Predictions for high heat fluxes exist for tokamaks under certain conditions [1]. Minor heating of wall elements by fast ions generated from external heating sources has been observed in a previous campaign of the stellarator Wendelstein 7-X (W7-X) [2], after modifications were made to prevent potential damage.

In a tokamak device, fast ions are initially well-confined due to the axisymmetric configuration, which always aligns the drift surfaces with the magnetic flux surfaces. This is not the case for stellarators, as they are by concept non-axisymmetric. Thus, other approaches need to be taken to ensure fast particle confinement. The most critical class of particles here is that of trapped particles, as these cannot average out their radial drift velocity through full poloidal precessions. The motion of these particles in W7-X, which drift

* Author to whom any correspondence should be addressed.



Original Content from this work may be used under the terms of the [Creative Commons Attribution 4.0 licence](https://creativecommons.org/licenses/by/4.0/). Any further distribution of this work must maintain attribution to the author(s) and the title of the work, journal citation and DOI.

predominantly in toroidal direction with poloidal precession [3], stands in contrast to trapped (banana) particles in tokamaks, which drift predominantly poloidally and precess toroidally. In W7-X, the so-called quasi-isodynamic behaviour is predicted to improve confinement of these particles for high plasma pressure gradients [4], which are present at high β -values. Achieving this behaviour was one of the optimization goals in the conceptual phase of the machine [5].

To validate this improvement in confinement, a host of diagnostics is needed. The one of interest for this work is the in-wall tile fast ion loss detector (FILD), based on the Faraday cup principle, i.e. capturing fast ions on a conductor and measuring their current. A Faraday-cup based FILD has been previously constructed at the JET tokamak [6], based on thin metal membranes as active elements. The active elements of the detectors in development for W7-X are constructed by thin film deposition methods [7]. This allows for a form factor of the size of a microchip ($39 \times 25 \times 5$ mm). The small footprint allows a detector of this kind to be embedded in the standard carbon wall tiles, giving substantial freedom in the placement within the vessel. Furthermore, this allows the construction of a distributed low-resolution array of these detectors, which is essential to measure differences in hot spots due to magnetic configuration or plasma parameter changes (see figure 1). The detector distinguishes relative fractions of energy levels by different deposition depths. Different thicknesses of insulating material are applied above the conducting layers, the active element then corresponds to the deposition depth of particles of a chosen energy range. The detector has five conducting fingers and the insulating layers are applied in a staircase pattern, giving flexibility to tune the individual layer thickness above each finger while ensuring good insulation from one finger to the next and to the underlying substrate. Thus, the particle flux from five energy ranges can be measured. A broad selection of particle pitch is also possible through the aperture geometry, although it is shown in this work that most given spatial positions at the first wall have a narrow pitch distribution.

The freedom in positioning the detectors for the array requires a detailed study of the fast ion losses for different cases to determine the optimal configuration. Therefore, simulations are investigated here, based on neutral beam injected particles. These particles are seen, by orbit scaling arguments, as proxies for α -particles in a reactor based on W7-X. The neutral beam injection (NBI) system in W7-X generates particles in the 10–100 keV range. It is currently the main method of generating fast particles, so it is a natural starting point for assessing FILDs in W7-X.

In this work, an array of the in-wall tile fast ion loss detectors will be presented, which shows good representation of the global loss fraction observed in simulations. The configuration is based on NBI simulations and multiple plasma pressure (β) values as well as magnetic configurations.

1.2. Magnetic configurations in W7-X

The magnetic field of W7-X is generated by 20 planar and 50 non-planar superconducting coils. In each of the five modules

(field periods), which are identical from a magnetic standpoint, four planar and ten non-planar coils are present, divided into two half-modules. The non-planar coils generate the characteristic stellarator magnetic field, while the planar coils are used to achieve different magnetic configurations through current variations. The coils of each field period are connected in series, such that the current through each group of the same type of coil is equal. The configuration where the planar coils are switched off and the current through all non-planar coils is equal is called the standard configuration. In the context of this work, the high iota and high mirror are furthermore important. The high mirror configuration is the most interesting, as is predicted to achieve the quasi-isodynamic effect for high plasma pressures. It is thus the focus of this work. The currents in the planar and nonplanar coils for the three magnetic configurations relevant to this work can be found in table 1.

Considering the shape of the magnetic field, the following can be said: the highest magnetic fields in the configurations under investigation appear at the bean-shaped cross-section in the middle of each module. The lowest fields conversely occur at the triangular cross-section at the module ends. This toroidal variation in field strength causes particles to mirror predominantly at or near the bean-shaped cross-section, making them toroidally trapped under the appropriate conditions.

1.3. Particle orbits in W7-X

The condition under which particles can be considered trapped and thus exhibit quasi-isodynamic behavior if they are also collisionless can be characterized by the mirror magnetic field. This is the magnetic field strength where the parallel velocity of the particle vanishes and it reverses its direction. It is easily calculated using the kinetic energy and magnetic moment, or alternatively the local magnetic field and velocity components. At the mirror position $v = v_{\perp}$ and thus

$$B_{\text{mir}} = B \frac{1/2mv^2}{1/2mv_{\perp}^2} = \frac{E_{\text{kin,mir}}}{\mu} = B \frac{v^2}{v_{\perp}^2} \quad (1)$$

where B is the local magnetic field, m is the particle mass, v_{\perp} its velocity perpendicular to the magnetic field, and $E_{\text{kin,ref}}$ the kinetic energy. The subscript indicates that in the reflection point, all kinetic energy is perpendicular to the field. As both the kinetic energy and magnetic moment are conserved quantities in an adiabatic field, collisionless particle orbits can be classified according to B_{mir} [8].

Particles with mirror field higher than in the bean-shaped cross-section are never reflected (passing particles) and are collisionlessly confined. If the mirror field is lower than the maximum field in the bean cross-section the particle is considered barely passing, as it can pass through some sections of the bean and go from one field period to the next. Deeply trapped particles are those with mirror fields lower than the minimum in the bean, as these are always reflected before entering the next field period.

The high mirror configuration of W7-X was designed for fast particles close to the magnetic axis [9]. As can be seen in

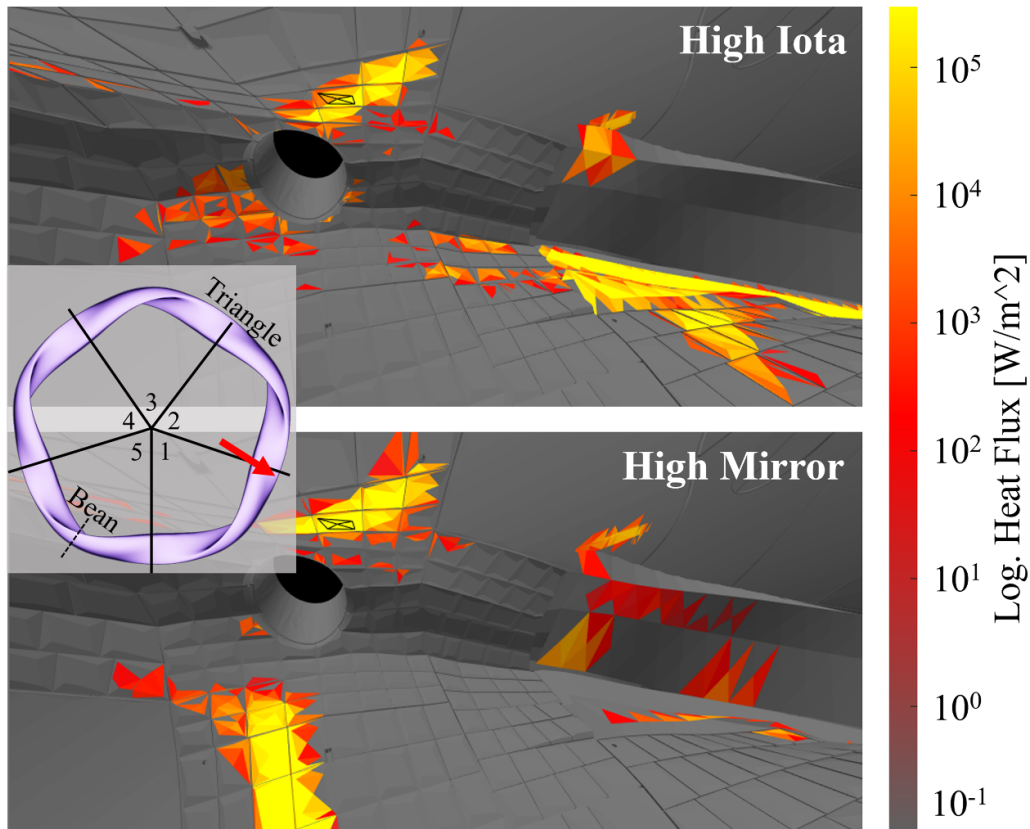


Figure 1. Heat flux generated on the first wall of W7-X by lost fast ions for high mirror and high iota magnetic configurations. Otherwise equal parameters (see table 2). See following sections for simulation methods. The comparison shows the large influence the magnetic configuration has on the hot spot locations. The inset shows the plasma shape of W7-X, divided into five modules. Positions of bean-shaped and triangular cross-sections are indicated, which both adhere to the five-module symmetry. The view direction of the main figure is indicated by the red arrow.

Table 1. Values of coil currents for the three different magnetic configurations considered in this work.

Configuration	Nonplanar coils (A)					Planar coils (A)	
	I_1	I_2	I_3	I_4	I_5	I_A	I_B
Standard	12 985	12 985	12 985	12 985	12 985	0	0
High iota	14 188	14 188	14 188	14 188	14 188	-9790	-9790
High mirror	13 230	12 859	12 251	11 642	11 272	0	0

figure 2(a), the contours of magnetic field strength close poloidally for the high mirror configuration at high beta close to the axis. All particles trapped in the toroidal mirror are confined as they mirror at equal toroidal angles and cancel their radial drift through poloidal precession in the so-called quasi-isodynamic behavior. This is not the case for further out flux surfaces, also visible in figure 2(b). Here, the magnetic field can vary considerably in a poloidal section, and the toroidal mirror is consequently not independent of the poloidal position. Particles can thus trap and de-trap collisionlessly, as they encounter different field strengths depending on their current poloidal position. If their mirror field is low enough, they will always mirror before the bean-shaped cross-section, at different toroidal positions and confining them to a region with roughly equal curvature. This can cause them to drift outward incrementally and traverse flux surfaces.

2. Methods

The goal of this work is to determine the most promising sensor positions for the new in-wall tile FILD [7] for measuring fast ions generated by the W7-X NBI system [10]. Currently, the NBI system injects hydrogen atoms at 55, 27.5 and 18.3 keV with fractions of 54.6%, 30.9% and 14.5%. H_2^+ and H_3^+ molecules are co-extracted from the NBI sources together with atomic hydrogen, causing the different energy levels. Monte Carlo method-based simulations are performed to determine the locality of the fast ions hitting the vessel wall for different magnetic and plasma configurations. A simulation framework with BEAMS3D [11] and ASCOT5 [12, 13] at its core is employed, which will be introduced in detail in this section. Using the ion distributions obtained, detector positions can be determined which reproduce the

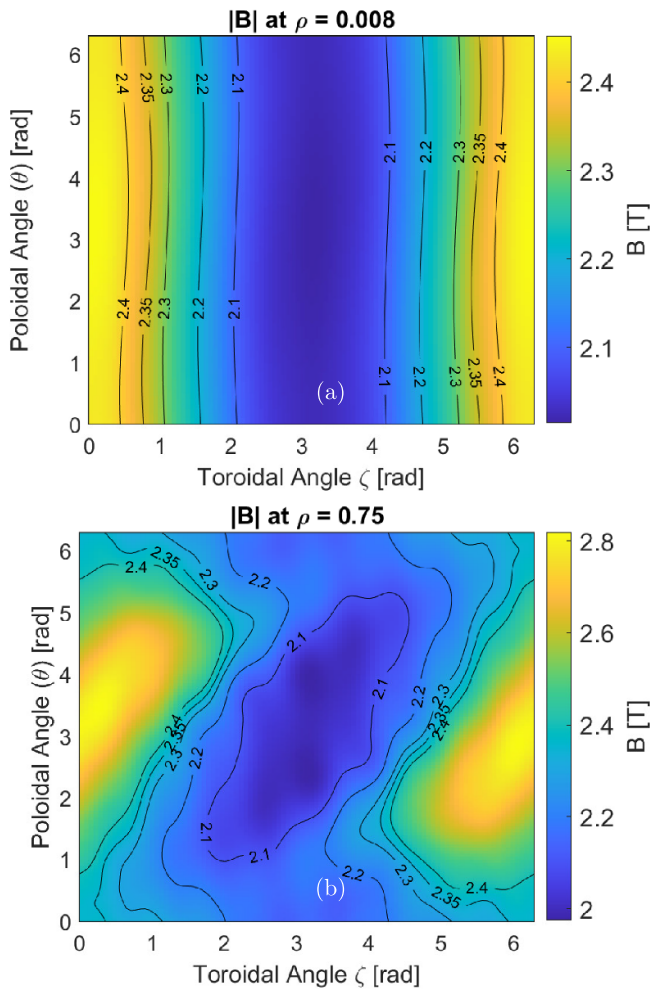


Figure 2. Magnetic field strength at the flux surfaces (a) $\rho = 0.008$ and (b) at $\rho = 0.75$ for a $\beta = 3.6\%$ equilibrium in the high mirror configuration. ζ is the toroidal angle spanning one field period. The coordinate origin is located at the outboard midplane at the beam-shaped cross section.

global loss pattern as well as special features, such as the quasi-isodynamic effect.

2.1. Workflow overview

The workflow used here and the codes comprising it are depicted in figure 3 and described in the following. Simulations were carried out on clusters consisting of 40 Intel Skylake cores per compute node. The computational (wall clock) time for a typical simulation (run b in table 2) was 8 min for the deposition on 16 nodes, 3.5 h for the slowing down run on 64 nodes and 9.5 h on 128 nodes for the full orbit wall collision run.

The density and temperature profiles are taken from a database of DKES simulations for W7-X [14] and are used together with the coil filament geometry to generate the input file for BEAMS3D. Here, the radial electric field as well as neoclassical particle flux estimates are calculated with NEO-TRANSP [15]. VMEC generates the equilibrium used in the

subsequent simulations. Next, in the neutral beam deposition simulation, the geometry of the port and beam dump as well as the individual beamlet geometries are taken into account. This first simulation also generates the base input file for ASCOT5, using an interface to transfer all quantities, as has been done in a previous work [16]. The markers, representing confined ions are then taken into another BEAMS3D simulation, propagating them through the slowing down process until they reach the last closed-flux surface (LCFS) or thermalize. This simulation is based on the gyro-center equations of motion. The lost markers are then selected and multiplied, and the full orbit ASCOT5 run is started with a slightly different wall model better suited for wall losses in the whole torus. This results in a detailed wall loss distribution of the fast ions, which can be used to determine the detector output, but also e.g. heat fluxes at the wall. This approach uses the strengths of each code: BEAMS3D has been validated for its NBI particle deposition in W7-X [17], and its slowing down behavior has also been investigated [16]. ASCOT5 has full-orbit capabilities, which is important for precise wall hit positions. Additionally, it uses an octree data structure to detect wall collisions, permitting more markers in the simulation. The (triangular) wall meshes used in this work are based on the CAD models of W7-X with some modifications in port and divertor areas and have around 5 million mesh elements. The surface area of the triangular mesh elements varies widely in a range from 0.1 cm^2 to 500 cm^2 .

The simulations presented here give results for the steady-state fast ion distribution. As such, time-dependent phenomena such as Alfvénic activity and instabilities requiring additional code development are left to future work. The radial electric field as well as collisional effects resulting from neutral as well as electron and ion densities are excluded in the simulations outside the last closed flux surface. This is due to large uncertainties associated with these quantities in the edge region at this time. Specific diagnostics are currently being developed, their data will likely become available in the future.

2.2. Injection and slowing down simulations with BEAMS3D

BEAMS3D is a Monte Carlo particle following code for neutral beam injection and orbit following of fast ions in stellarators. The neutral particle trajectories are simulated as straight lines, using the provided wall geometry to detect collisions and plasma profiles for ionization probabilities. The code is interfaced to the Suzuki database [18] to determine ionization cross-sections. Around 1.5 million markers were injected in each simulation, corresponding to a particle flux of $2.5 \times 10^{21} \text{ s}^{-1}$. All eight NBI sources were active in the simulations and considered in the results. The geometry of the NBI sources with respect to the plasma as well as the radial birth profiles can be obtained from figure 4. As explained in the previous section, BEAMS3D uses gyro-center equations of motion for the slowing down simulation of the ions. The birth positions are determined from the ionization location and applying a step to the gyro-center with random gyro-phase. The equations for following the particles are

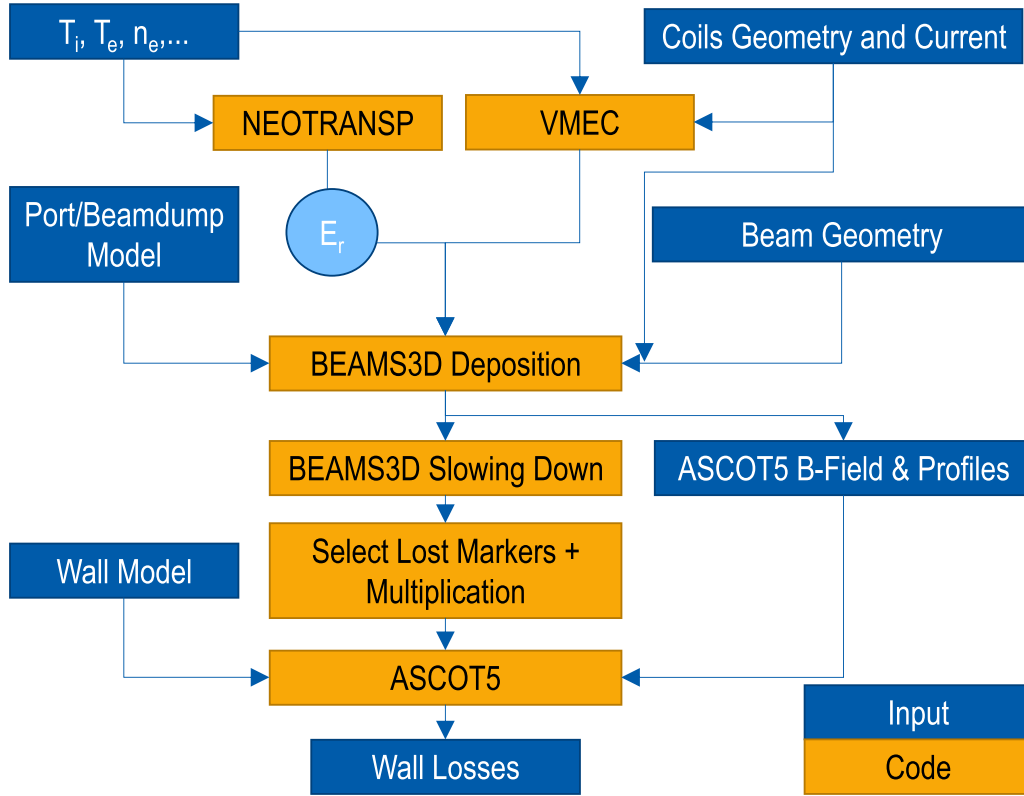


Figure 3. Overview of the codes employed to simulate NBI-generated fast ions.

$$\frac{d\vec{R}}{dt} = \frac{\hat{b}}{qB} \times \left(\mu \nabla B + \frac{mv_{\parallel}^2}{B} (\hat{b} \cdot \nabla) \vec{B} \right) + v_{\parallel} \hat{b} + \frac{\vec{E} \times \vec{B}}{B^2} \quad (2)$$

$$\frac{dv_{\parallel}}{dt} = -\frac{\mu}{m} \hat{b} \cdot (\nabla B). \quad (3)$$

Here, $\hat{b} = \vec{B}/B$, $\mu = 1/2 \frac{m_{\perp}^2}{B}$ is the magnetic moment, $\vec{E} = -\nabla\Phi$ the electric field, $v_{\parallel} = \frac{d\vec{R}}{dt} \cdot \hat{b}(\vec{R})$ is the velocity component parallel to the magnetic field [17]. The field quantities (\vec{B} and Φ) are represented on cubic Hermite polynomial splines (C1). In this work, the cylindrical grid upon which these splines are constructed has 128 radial, 128 vertical and 36 toroidal grid points. Its extent spans $R = [4.5, 6.5]$ m, $Z = [-1.5, 1.5]$ m, and $\phi = [0, 2\pi/5]$ rad in the radial, vertical and toroidal directions, respectively. The toroidal extent is over one field period, and the quantities are later used in the full field using periodic boundary conditions. BEAMS3D takes the magnetic field components inside the LCFS from VMEC and calculates the field outside under vacuum field assumption from the plasma and coil currents. A virtual casing principle is employed for the field arising from plasma currents [19]. The aforementioned cylindrical grid is also used for the electron density and temperatures (electron and ion) as well as the effective charge number.

The usual maximum simulation time for the simulations presented here was 100 ms, equating to 2–3 times the equilibration time for the fast ion distribution function, after which all particles are thermalized. Thus, hardly any particles reached

this maximum simulation time, which is required for confidence in the results.

Additionally, to the motion in the magnetic field, the effects of pitch angle scattering and slowing down are calculated on a per species basis. The code calculates the local collisionality by using the plasma quantities at the marker position (density and temperature). The collisionality, based here on the Spitzer ion-electron momentum exchange time, approximately scales with the plasma parameters as $\nu_s = 1/\tau_s \propto n_e T_e^{-3/2}$. Additionally, for the slowing down simulations, a virtual wall surface is constructed at the location of the LCFS to detect particles leaving the plasma. For this work, this virtual wall had vertices at 180 toroidal and 120 poloidal positions over the full torus.

2.3. Simulating escaping particles with ASCOT5

Taking the markers exiting the LCFS, ASCOT5 follows the full orbit of the simulation markers adhering to the well-known equations of motion of charged particles in a magnetic field

$$\dot{\vec{v}} = \frac{e}{m} (\vec{E} + \vec{v} \times \vec{B}) \quad (4)$$

$$\dot{\vec{r}} = \vec{v}, \quad (5)$$

where e is the elementary charge, \vec{r} is the particle position and all other quantities are standard. The propagation in time is done via a fixed timestep, energy, and relativistic volume preserving algorithm [13].

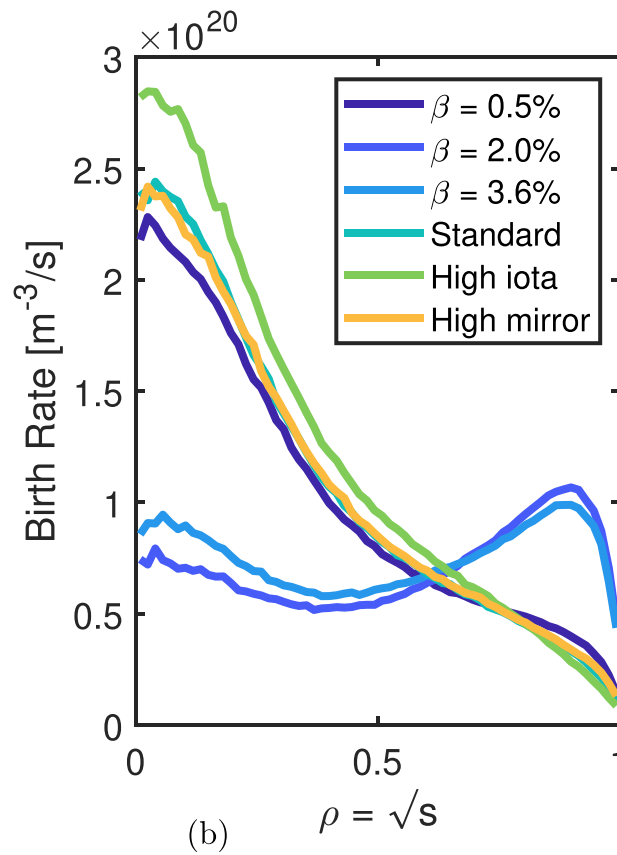
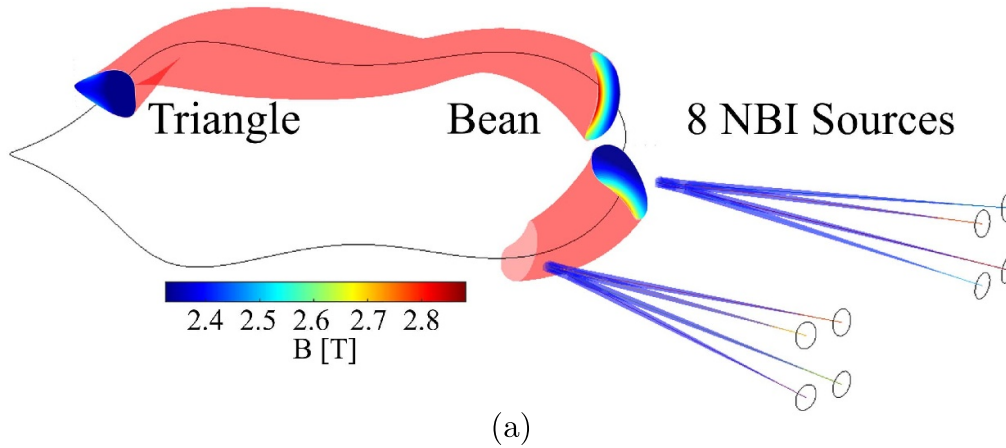


Figure 4. (a) Schematic of the eight NBI sources simulated in this work. The bean and triangular shaped cross-section as well as the cross section at the injection location are indicated with respect to their magnetic field. (b) NBI deposition profiles for the runs presented in this work, see table 2 for details. The first three cases are in the high mirror magnetic configuration.

ASCOT5 uses a similar cylindrical grid as BEAMS3D for the representation of field quantities. It spans $R = [4.25, 6.5]$ m with 256 grid points in the radial direction, $Z = [-1.25, 1.25]$ m with 256 grid points in the vertical direction, and $\phi = [0, 2\pi/5]$ rad with 71 grid points in the toroidal direction. For the full orbit simulation, a step size of $1/16$ th of the gyro frequency was chosen which yielded good results in earlier simulations while not being overly computationally expensive. Typical marker counts for the simulations

presented here were of the order of 4 million markers. The multiplication step arriving at this number from BEAMS3D is described in the following section 2.4.

The simulations with ASCOT only consider the magnetic field calculated by plasma and coil currents from BEAMS3D. No pitch angle scattering, friction or radial electric field are taken into account. Furthermore, the effect of charge exchange reactions is not implemented in the challenging 3D geometry, although work is ongoing in this regard.

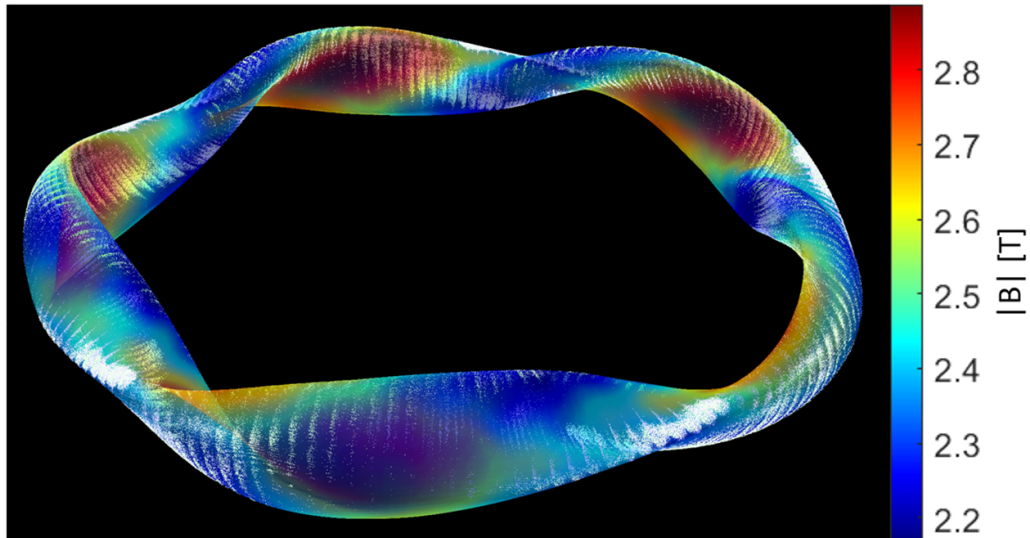


Figure 5. Marker positions at the LCFS (white). The underlying magnetic field is indicated by color. Spots of increased marker density are visible at the triangular cross sections on the outboard side.

2.4. Marker multiplication

The markers as simulated by BEAMS3D are processed before the ASCOT simulation is started. First, only the markers exiting the LCFS are selected to be simulated, see figure 5. These markers are then multiplied to increase the hit statistics on the wall. The marker weight, in units of $[\text{particles s}^{-1}]$, is decreased to keep the total particle flux constant. In the case of the simulations presented a multiplication factor of 16 was used, in a balance between marker count and simulation time. A small perturbation in the pitch angle of the marker is also applied during the multiplication, visible in the inset of figure 6. In effect, the multiplied markers have slightly different velocity vectors (the original marker is always retained). This yields a more even distribution in velocity space and leads to less outliers of mesh elements with high heat flux, caused by a single marker. A perturbation of 5% for the pitch angle was used throughout this work. A preliminary scan of this perturbation, ranging from 0% to 64% showed no significant difference in regions of high marker count. The gyro-center positions from BEAMS3D are then converted to particle positions by performing a step the size of a gyro radius and random gyro phase.

2.5. Simulation run overview

In this work, we investigated cases with achievable plasma parameters, based on experience from previous campaigns. A scan of plasma β ranging 0.5%–3.6% was performed, and a configuration scan investigating the standard, high iota and high mirror configurations. An overview of the parameters of each simulation is given in table 2. The temperature and density profiles approximate realistic profiles of ECRH shots with NBI. In figure 7, they can be seen for the first three runs (a–c). The increase in plasma β was realized by first stepping up the plasma density to quadruple its original value, increasing the collisionality and decreasing shine-through of

the NBI particles. The next step was in electron temperature, also increasing plasma pressure but decreasing collisionality almost to its original value and keeping shine-through practically unchanged. For the configuration scan, the plasma parameters were kept as similar as possible. Thus, collisionality, plasma pressure and shine through of the neutral beam are almost identical between runs (d–f). The high iota run has marginally higher shine through.

3. Results

The detector positions presented here were found in an iterative procedure and will be demonstrated to fulfill the requirements of being able to reproduce the global loss fraction. The global loss and thermalized fractions are given in table 3 as reference. Peculiarly, and in seeming contrast to the predictions of quasi-isodynamicity, the loss fraction increases with β . This behavior can be explained by the type of orbits the NBI populates, caused by the injection geometry. The type of particle that is generated is not predicted to express the quasi-isodynamic effect. This will be further explained in the discussion section. The fractions in table 3 are given with respect to the initial injected markers, comparing markers before they enter the plasma to those that, e.g., exit the LCFS. This would include an increase in deposited fraction. We see that this fraction nearly doubles when going from low to high β . When we now consider the loss fraction calculated with respect to the deposited/ionized particles, it still increases from 7.4% ($\beta = 0.5\%$) to 12.9% ($\beta = 3.6\%$). The majority of the loss increase thus is not caused by a changing/increased NBI deposition. To explain the results of the high-mirror configuration simulation (f) having a higher loss fraction than any of the runs in the β scan, one needs to consider two effects: pitch-angle scattering, driven by an increase in T_e , and slowing down, driven by the density. In run f, T_e is high while the density is low, so even passing particles can spontaneously be

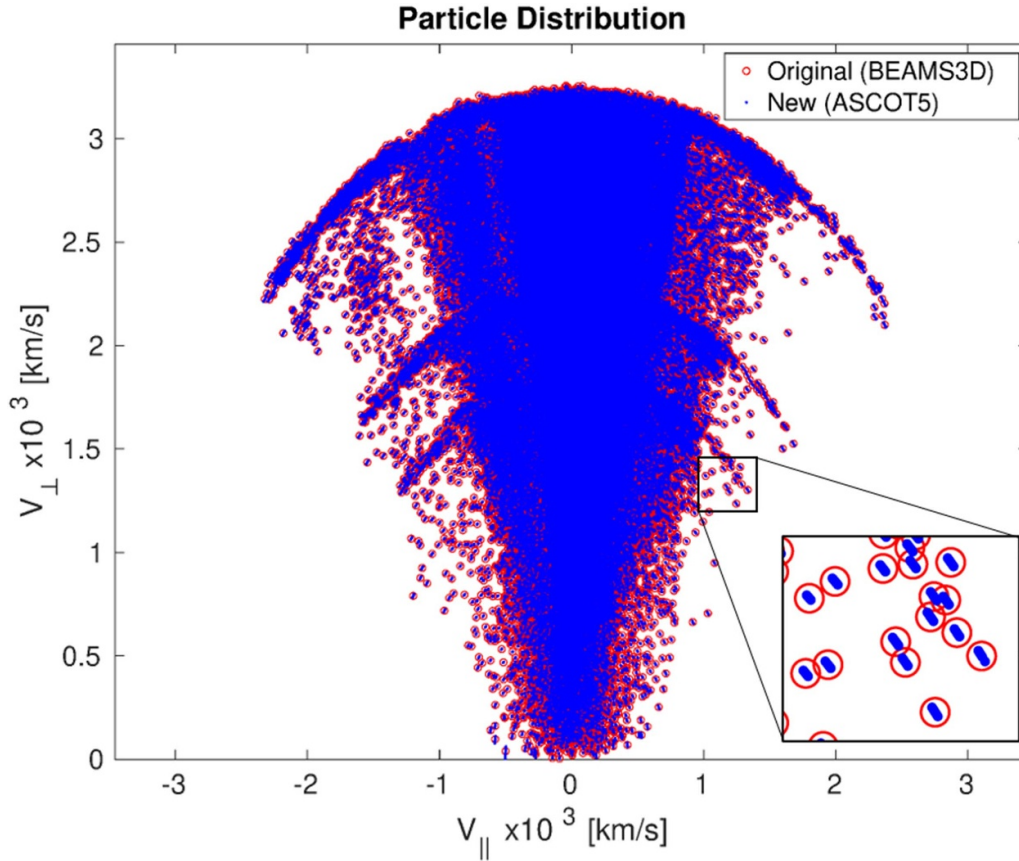


Figure 6. Velocity space of marker multiplication for particles at the LCFS. Each original marker from BEAMS3D is multiplied 16 times with a small pitch angle perturbation, resulting in ‘smearing’ of the ASCOT5 markers in the inset. The three semi-ring structures represent the full, half and third NBI energies, made visible through prompt losses.

Table 2. Parameters of the simulations presented here. Ion temperature is clamped to max. 1.6 keV.

Run	Mag.-Conf.	n_e (m^{-3})	T_e (keV)	T_i (keV)	Edge ι	Mirror ratio	β_{tot} (%)
a	High mirror	5×10^{19}	2.0	1.6	5/5	0.10	0.5
b	High mirror	20×10^{19}	2.0	1.6	5/5	0.10	2.0
c	High mirror	20×10^{19}	4.0	1.6	5/5	0.10	3.6
d	Standard	6×10^{19}	4.0	1.5	5/5	0.04	1.3
e	High iota	6×10^{19}	4.0	1.5	5/4	0.05	1.3
f	High mirror	6×10^{19}	4.0	1.5	5/5	0.10	1.5

trapped through pitch-angle scattering and will exit the plasma before thermalizing.

3.1. Global properties of the array

The low-resolution array consists of 16 detectors in total including three toroidal arrays of 5 detectors each. The ASCOT5 simulations predict a very even distribution of the lost particles over the field periods, and toroidal arrays are a good way to verify this. A subselection of the toroidal positions may also be sufficient if this verification is of lower interest. A perspective view of the detector positions, looking into negative toroidal direction from module 40 (first half-module of module 4), is given in figure 8. The cylindrical coordinates of the detector positions are given in table 4. The

markers hitting this detector array will be compared to all markers in the simulation, hitting any of the wall tiles.

The first requirement for the array is to reproduce the global loss fraction. To assess this, the particle flux (weight) of the global simulation is compared to the weight incident on the detector positions. The depiction of this comparison is visible in figure 9. The left and right vertical axis have different scales, as the detector array only picks up on average 0.55% of the total weight present in the simulation. The largest relative difference with respect to this value is 17%, observed in the $\beta = 3.6\%$ run. The experimental fraction of detected weight should be substantially lower, as no aperture effect is considered here yet, due to the detector design not being finalized. From the figure, we obtain that the array does reproduce the loss fraction qualitatively, except for the case of $\beta = 0.5\%$.

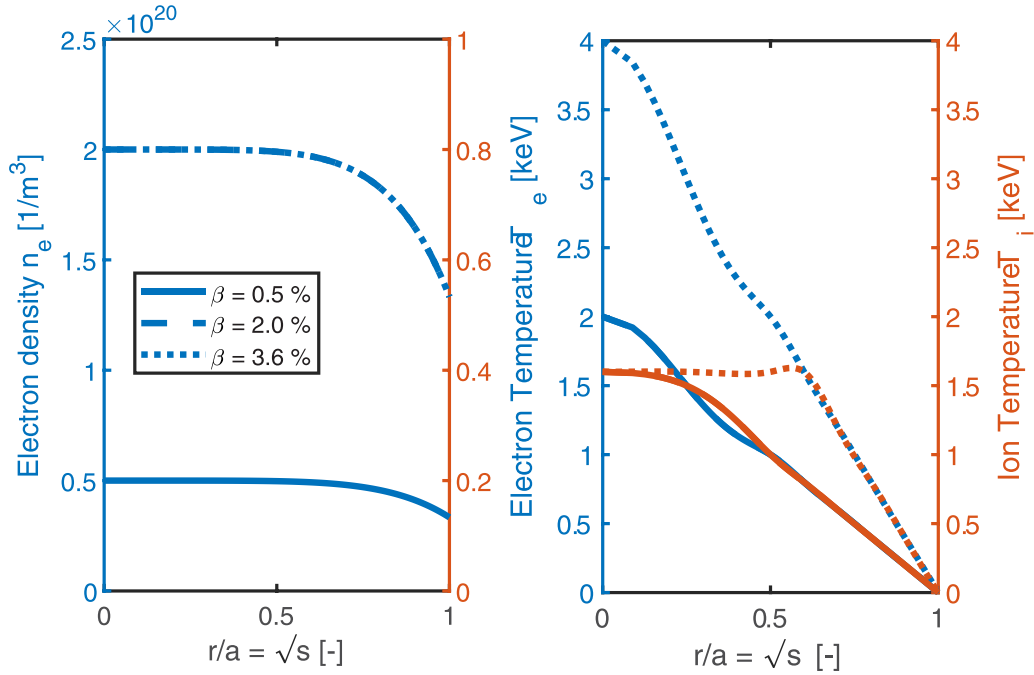


Figure 7. Temperature and density profiles for runs a–c in table 2. They represent an approximation to stereotypical parameters in a W7-X discharge.

Table 3. Global results of simulations. Wall loss and thermalized fractions given w.r.t. particle flux before NBI injection. Note the increase in loss fraction in the first three runs, indicating that the particles do not behave according to quasi-isodynamicity.

Run	Mag.-Conf.	β_{tot} (%)	f_{loss} (%)	f_{therm} (%)
a	High mirror	0.5	5.6	70.2
b	High mirror	2.0	6.0	79.4
c	High mirror	3.6	11.0	74.4
d	Standard	1.3	16.2	61.0
e	High iota	1.3	17.2	57.6
f	High mirror	1.5	12.8	64.6

This is due to the array indicated by ‘D’ in figure 8 being especially sensitive to deeply trapped losses, as it is located in a region of low field strength (inboard side close to triangular cross-section) and negative geodesic curvature. Removing this toroidal array from the analysis results in a qualitative reproduction of the β scan (runs a–c) at the expense of the reproduction of the configuration scan (runs d–f).

3.2. Detector output analysis

The detector measures particle flux through the Faraday effect and can distinguish energy levels by using the absorption depth of the particles. An investigation into the energy distributions at the detector locations is shown in figure 10. It shows that for all detector positions the peak of the distribution where the highest marker counts are slightly below 20 keV. Only the high-iota (e) configuration has a secondary peak in its distribution for position ‘D’ for energies slightly below the full injection energy, indicating prompt losses at this location and configuration.

The output currents of each detector can be determined from the simulation using the weight of the markers at the respective position, multiplied by their charge. Binning the markers by their energy before summing over them results in a complete prediction of the output of the later detectors. Figures 11 and 12 show this analysis for the first and second set of simulations, separated for clarity. Each individual bar in the figure stands for the output for a specific run, at a certain position. Each bar group thus represents a detector position for all included runs. The energy distribution is visible through the stacked section, colored according to the legend. The current predicted by the simulation is on the order of 1 mA, measurable even without extra amplifiers. However, closer analysis is necessary as effects with large impact such as charge exchange processes and material absorption models are not taken into account here. Estimating the charge exchange losses outside the LCFS, we estimate 60%–90% of the population will experience a reduction of 100 or less. This still makes the signal measurable using amplifiers. A part of the population will, however, be undetectable, as the estimated travelled distance of these particles is

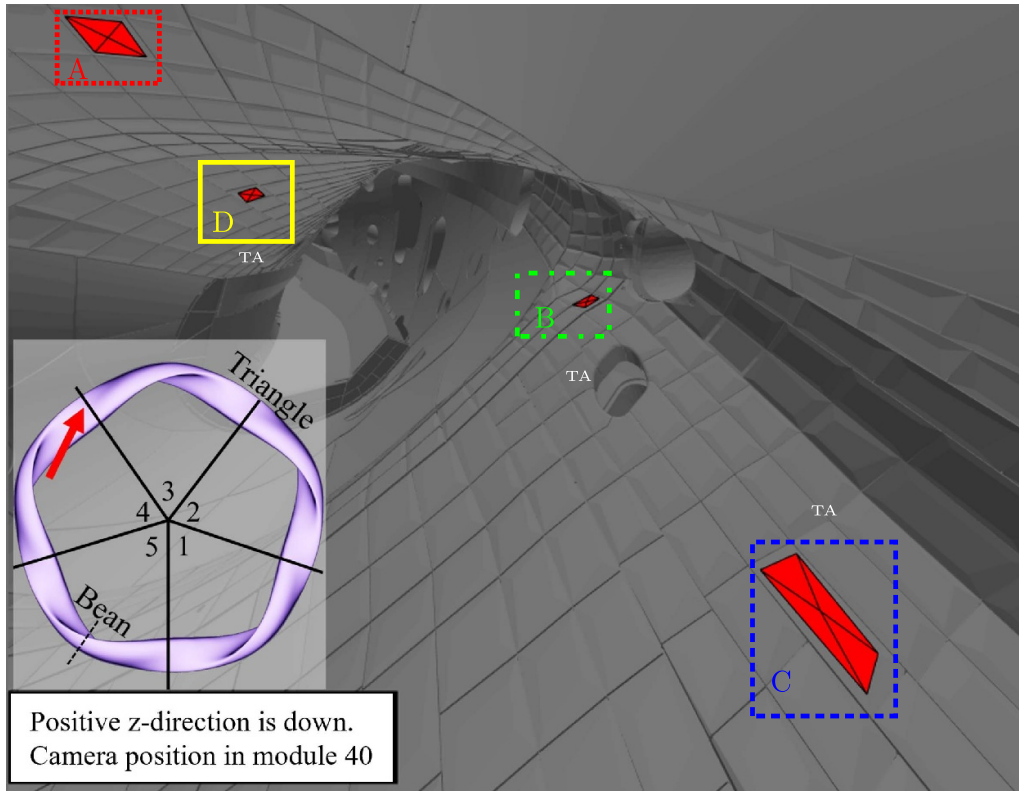


Figure 8. View of the detector positions. Different detector groups are enclosed by differently colored boxes. TA indicates a toroidal array of this detector. The inset indicates the position with respect to the plasma shape as in figure 1.

Table 4. Positions of the detectors in the (R, ϕ, z) cylindrical coordinate system. The toroidal coordinate is given with respect to a single module, in the range of $[0, 72]$ degrees. The range of values is given when the difference between positions is larger than the given digits.

Letter	R (m)	ϕ (deg)	z (m)
A	5.025	34.153	-0.563
B	6.095–6.100	34.542–34.730	0.162–0.192
C	6.051	41.091–41.112	0.364–0.365
D	5.043	25.210	-0.243

too large. For the estimation, we assumed a neutral density of $n_0 = 2 \times 10^{16} \text{ m}^{-3}$ and a hydrogen-hydrogen reaction cross-section of $\sigma_{\text{HH}} = 1 \times 10^{-11} \text{ m}^2$ for the energies under consideration.

The global trend of increasing loss fraction with increasing β value is visible in the ‘B’ and ‘C’ toroidal arrays of figure 11. The ‘A’ sensor and ‘D’ toroidal array (both closer to the inboard side) shows the inverse behaviour, decreasing their amplitude with β . From the simulations it is confirmed that toroidally trapped particles predominantly exit towards the inboard side around the triangular cross-section. Close to the triangular position, the magnetic field strength is nearly uniform with respect to the major radius with a slight increase towards the outboard side, visible in figure 4(a). Thus, toroidally trapped particles orbiting mainly in this area appear closer to the inboard side. In the ‘B’ array, the differences between

individual toroidal positions are most pronounced, which is due to the wall geometry changing substantially depending on the presence of a magnetic diagnostic loop and its shielding. This construction is used to shield e.g. magnetic diagnostics from the plasma, which have to be mounted inside the vessel. For the two highest amplitudes, this structure is missing, and the steel panels coming from the divertor are extended. A large portion of the increase comes from particles close to the injection energy, i.e. prompt losses that occur on short timescales before the particles have slowed down.

The configuration dependence of losses observed in figure 1 is also clearly visible in figure 12, as every detector position has a distinct response in the different simulations. The ‘B’ and ‘C’ marked positions, which have a similar poloidal position are vastly different when comparing the amplitude of the high iota run to the other two runs. This difference is partly discernable in figure 1. The energy ratios at each position stay roughly constant throughout the simulations. The similarity within the ‘C’ and ‘D’ arrays respectively indicates that a reduction of positions could be possible, depending on installation complexity, cost and experimental goals.

3.3. Phase space analysis

For further refinement of the array and in light of a future tomographic reconstruction of the fast ion distribution function, the phase space observed by the detectors is presented in figure 13. It shows that the array sees mainly trapped particles, although it should be noted that particles arriving

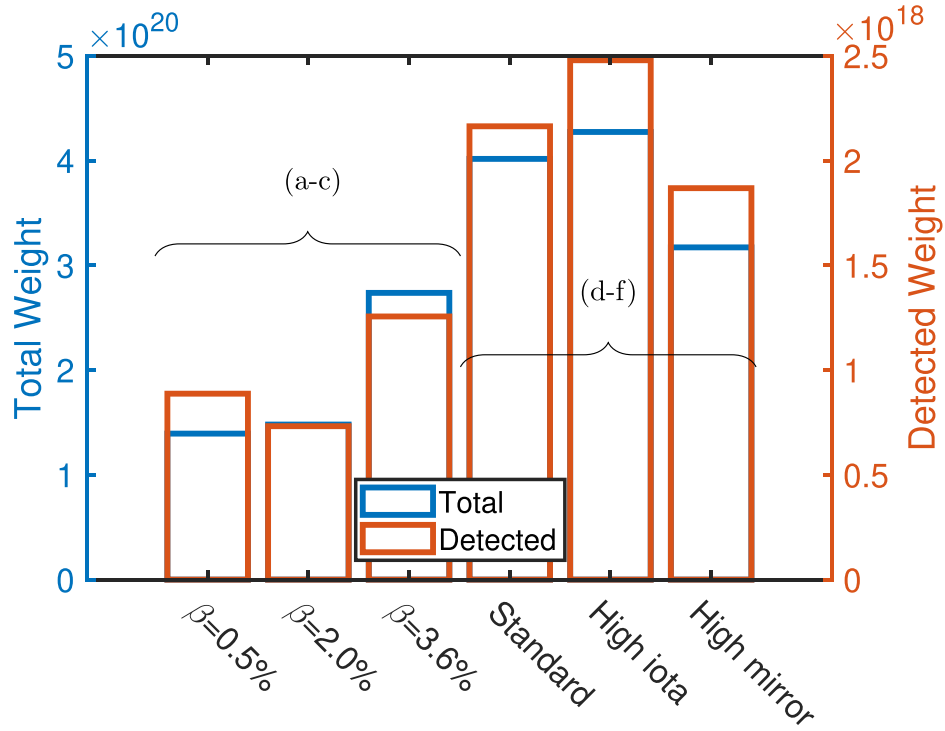


Figure 9. Comparison of detected to global lost marker weight (particles s^{-1}) for each simulation. Note the different scales for the vertical axes.

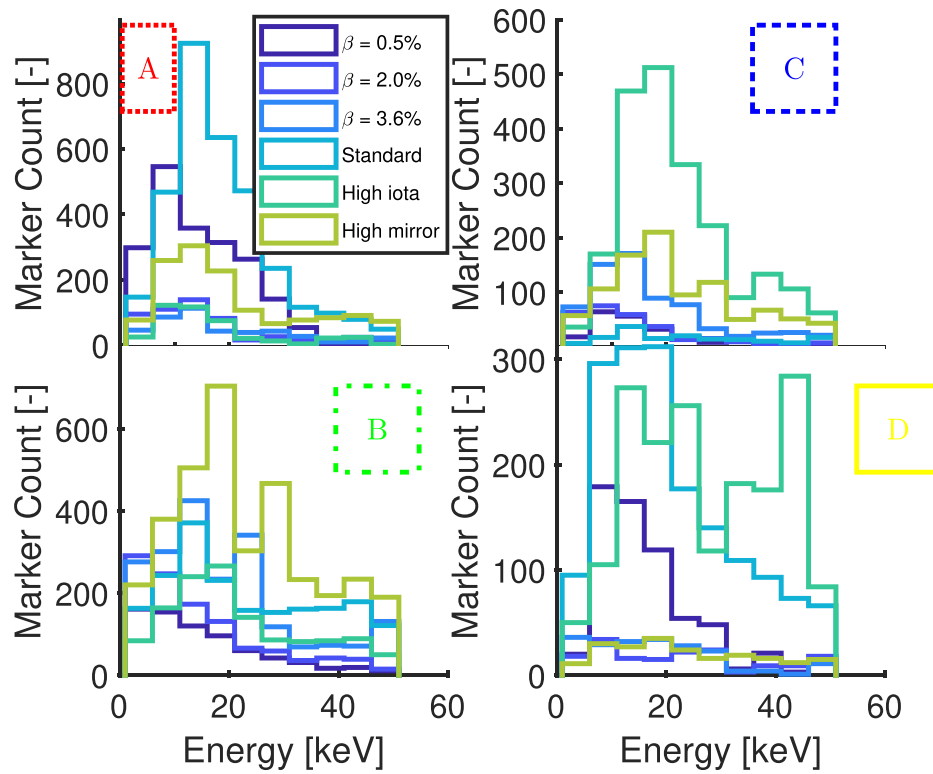


Figure 10. Energy distribution of a representative detector of each group shown in figure 8 for all simulated cases. Generally, all detectors seem to have a peak in their distribution around 20 keV, but the maximum values are reached for different simulation runs. The first three cases are in the high mirror magnetic configuration. Details on the simulation parameters are found in table 2.

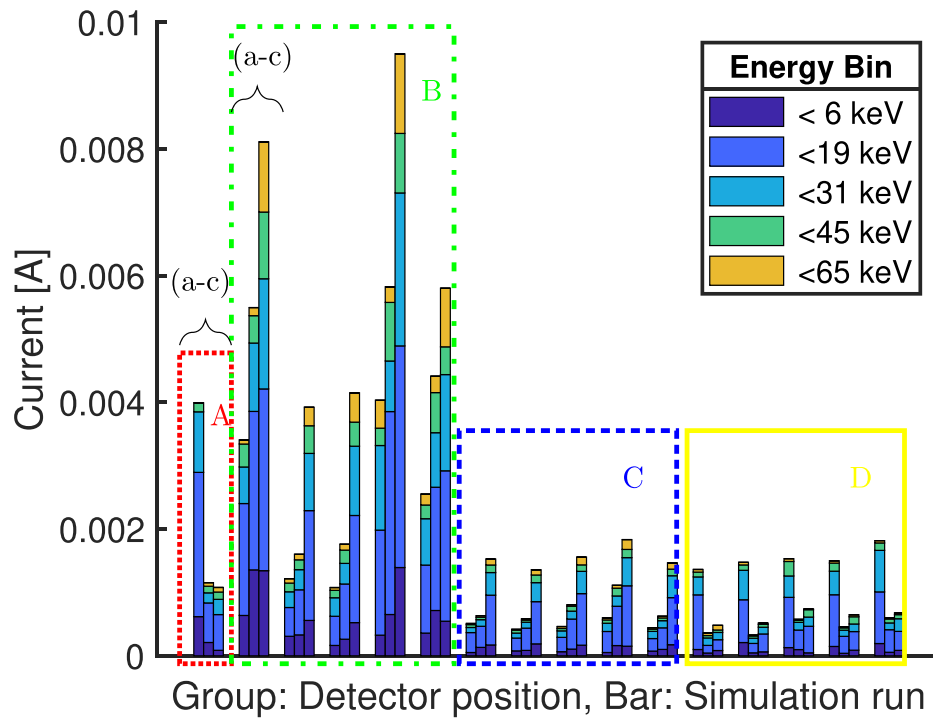


Figure 11. Current distribution for the energy bins and detector positions in the array, for the 1st set of simulations as shown in figure 9 (β scan). The three bars in each bar group represent the individual simulations (low to high β) at a specific position. The energy bins are centered around 12.5, 25, 50 keV, which are the design energies for the detector, and an intermediate range 31–45 keV.

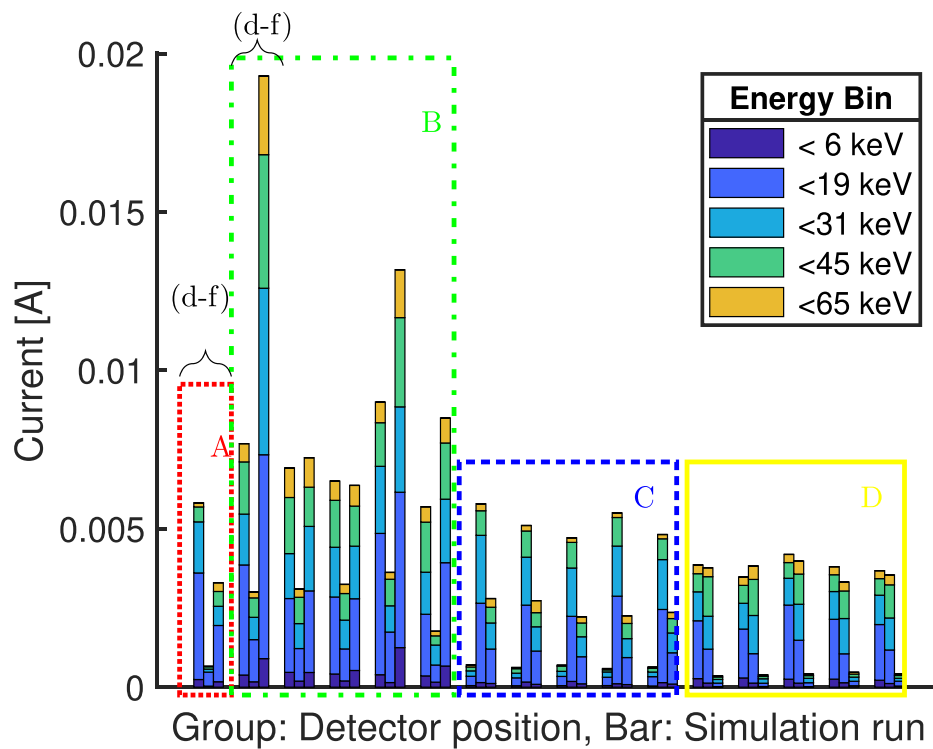


Figure 12. Current distribution for the energy bins and detector positions in the array, for the 2nd set of simulations as shown in figure 9 (configuration scan). The energy bins are centered around 12.5, 25, 50 keV, which are the design energies for the detector, and an intermediate range 31–45 keV.

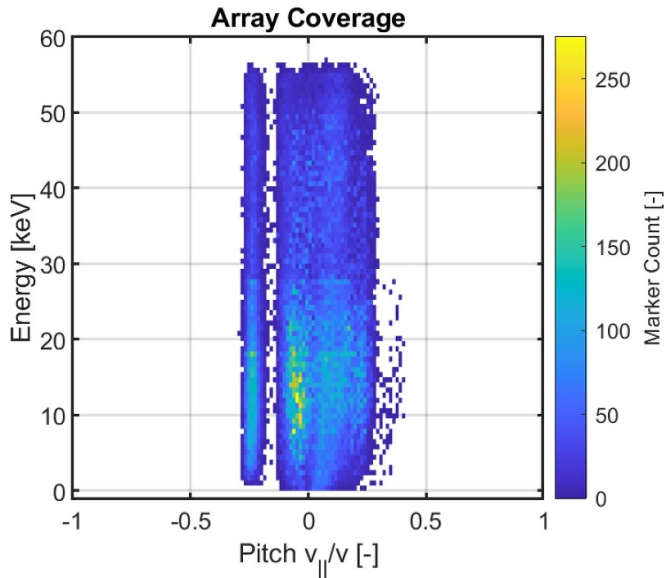


Figure 13. Phase space coverage of the proposed array. All simulations are included in the pitch-angle to energy distribution at the detector positions.

at the wall are mostly trapped in the ripple from the magnetic coils. Passing particles with high pitch mostly thermalize before they can reach the LCFS, thus figure 6 shows mostly low-pitch particles for the state going into ASCOT5. However, the pitch is a variable property throughout the orbit and changes at any given moment according to the local magnetic field strength. At the wall, hot spots of lost ions occur at local magnetic wells generated by the coil ripple. Another factor is the distance of the first wall to the plasma. Where the wall deviates from following the plasma shape and comes closer, particles can hit the leading edges. These have slightly larger pitch values and tend to spread out over larger areas. There are also array positions with both of these properties (sometimes in combination), because these positions experience loads in all configurations. The highest pitches in the simulations can be seen on the divertor and baffles. Steps in intensity can be observed at the half and third NBI energies (27.5 and 18.3 keV, respectively). A hot spot appears close to zero pitch and 15 keV energy, in accordance with the peaks observed in figure 10. It is generated by the overlap of the slowed down particles from all NBI energies. The location of this hot spot shows that in general significant slowing down takes place before the particles exit the plasma and hit the wall, especially considering that the third energy (18.3 keV) has the least fraction of initial power. The array seems to have a ‘blind spot’ at a pitch value of -0.15 . This is caused by the individual detector positions, each of which observes only a narrow pitch range. The range is determined by the location and angle of the wall tiles within the local mirror of the particles.

4. Discussion

As mentioned before, the rise of loss fraction with plasma β can only be explained by considering the particles the neutral

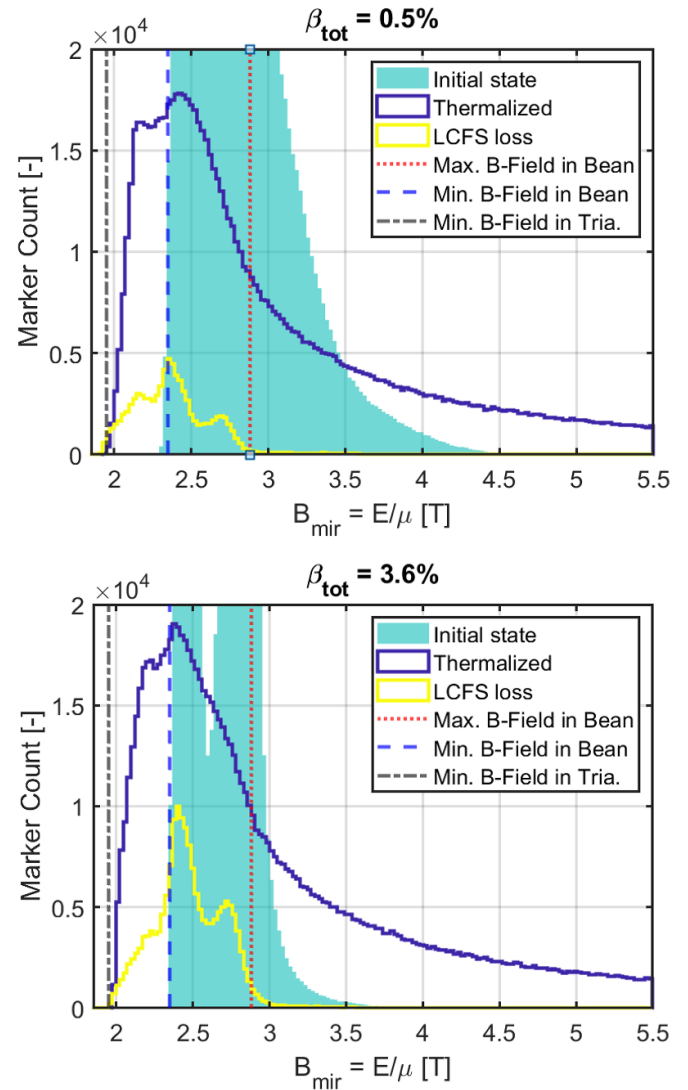


Figure 14. Spectra in B_{mir} of the initial injected fast ion population (high mirror configuration), as well as the thermalized and escaping populations at the last closed flux surface. The initial state shows that the NBI does not inject deeply trapped particles for either case.

beam system injects. Figure 14 shows the mirror field distribution for the simulated markers in the low and high β simulations. The trapped, barely trapped and passing regions are distinguishable from left to right by the vertical lines for minimum and maximum B-field in the bean shaped cross section. The distributions for initial state of the ions after injection show that in both cases, the NBI does not generate an appreciable amount of trapped particles. This can be considered a design feature, as trapped particles are by far not as well confined in W7-X as barely passing or passing particles. Thus, the injection of the latter (trapped) types of particles permits the use of the NBI as heating system, which is its main use case. The observed distribution arises from the proximity of the NBI to the bean shaped cross section. More precisely, the high magnetic field at the injection plane and a significant velocity component in the tangential direction set the minimum for the mirror field of the particles, evidently excluding

the deeply trapped region. It should be noted that the energy of the injected hydrogen particles is 55 keV, lower than the critical energy $E_{\text{crit}} = 15T_e = 60$ keV which would be required for them to experience equal drag from ions and electrons [20]. For deuterium, an energy of $19T_e = 76$ keV is necessary. This is generally considered to be the threshold for collisionless particles, although for applications a margin should be applied, particles should stay in the collisionless regime for a substantial time while slowing down. A value of 100 keV for $T_e = 4$ keV seems reasonable. The collisional behavior of NBI particles can be verified with the mirror field distribution of the lost particles at the LCFS in figure 14. It shows that a substantial portion of the losses is in the deeply trapped region, and was thus influenced by collisions after injection. The main increase in losses appears in the barely passing region. The distribution of other end conditions, mainly including thermalized particles, shows again a comparatively high contribution from deeply trapped particles generated by slowing down and pitch angle scattering, i.e. collisional effects.

The quasi-isodynamic effect might be shown with the current NBI system if the full distribution function could be measured, although low densities would be needed. The electron temperature would have to be balanced to have nearly collisionless particles at the NBI energy while slowing them down enough to observe the effect. A reconstruction of the full fast ion distribution with tomographic methods and data of multiple diagnostics will be attempted for W7-X in the future, making this a possibility if suitable plasma parameters are found. To measure the quasi-isodynamic effect directly and with greater certainty, a source of deeply trapped and collisionless ions is necessary. Preliminary work in this direction suggests this source should be close to the triangular cross-section, due to the low magnetic field, and with a substantially higher injection energy. Detailed analysis of this matter is left for a future publication.

5. Conclusion

A FILD detector array for Wendelstein 7-X has been presented, based on simulations of NBI particles. The simulations have been carried out using a combination of the BEAMS3D and ASCOT5 particle following codes. An array of detectors at the wall is necessary due to the hot-spot forming pattern, which drastically changes with magnetic and plasma configurations. With the proposed array configuration, the lost fraction can be reproduced qualitatively when comparing the different investigated configurations. The current output of the detectors seems adequate for measurements and might not need an amplifier if the predictions for the magnitude of the current hold true. In the case of budget or assembly constraints, a reduction of toroidal detector positions is possible. The detector array sees mostly locally trapped particles, as expected for a detector mounted at the first wall. The array is not expected to be able to measure the quasi-isodynamic behavior from the NBI particles, based on the simulations. Due to the high magnetic field at the injection location and relatively large deviation

from radial injection, the NBI does not generate deeply trapped particles, and its energy is too low to be considered collisionless. Therefore, combinations of diagnostics and tomographic methods for distribution construction may be necessary to see the effect. Alternatively, a source of deeply trapped particles could be constructed for direct measurement of these particles.





Data availability statement

The data that support the findings of this study are available upon reasonable request from the authors.

Acknowledgments

This work has been carried out within the framework of the EUROfusion Consortium and has received funding from the Euratom research and training programme 2014–2018 and 2019–2020 under Grant Agreement No. 633053. The views and opinions expressed herein do not necessarily reflect those of the European Commission. Computing resources for this work have been provided by the Max-Planck Computational Data Facility.

ORCID iDs

D Kulla  <https://orcid.org/0000-0003-1621-7338>
 S Lazerson  <https://orcid.org/0000-0001-8002-0121>
 D Hartmann  <https://orcid.org/0000-0002-3511-6500>
 R C Wolf  <https://orcid.org/0000-0002-2606-5289>

References

- [1] Duong H H, Heidbrink W W, Strait E J, Petrie T W, Lee R, Moyer R A and Watkins J G 1993 Loss of energetic beam ions during TAE instabilities *Nucl. Fusion* **33** 749–65
- [2] Äkäslompolo S et al 2019 Armoring of the Wendelstein 7-X divertor-observation immersion-tubes based on NBI fast-ion simulations *Fusion Eng. Des.* **146** 862–5
- [3] Nührenberg J 2010 Development of quasi-isodynamic stellarators *Plasma Phys. Control. Fusion* **52** 124003
- [4] Mikhailov M I, Shafranov V D and Nührenberg J 2009 Pressure insensitivity of a high- β quasi-isodynamic stellarator *Plasma Phys. Rep.* **35** 529–34
- [5] Wolf R C 2008 A stellarator reactor based on the optimization criteria of Wendelstein 7-X *Fusion Eng. Des.* **83** 990–6
- [6] Darrow D S, Bäuml S, Cecil F E, Kiptily V, Ellis R, Pedrick L and Werner A 2004 Design and construction of a fast ion loss Faraday cup array diagnostic for Joint European Torus *Rev. Sci. Instrum.* **75** 3566–8
- [7] Lazerson S A, Ellis R, Freeman C, Ilagan J, Wang T, Shao L, Allen N, Gates D and Neilson H 2019 Development of a Faraday cup fast ion loss detector for keV beam ions *Rev. Sci. Instrum.* **90** 093504
- [8] Faustin J M, Cooper W A, Graves J P, Pfefferlé D and Geiger J 2016 Fast particle loss channels in Wendelstein 7-X *Nucl. Fusion* **56** 092006
- [9] Drevlak M, Geiger J, Helander P and Turkin Y 2014 Fast particle confinement with optimized coil currents in the W7-X stellarator *Nucl. Fusion* **54** 073002

- [10] Rust N, Heinemann B, Mendelevitch B, Peacock A and Smirnow M 2011 W7-X neutral-beam-injection: selection of the NBI source positions for experiment start-up *Fusion Eng. Des.* **86** 728–31
- [11] McMillan M and Lazerson S A 2014 BEAMS3D neutral beam injection model *Plasma Phys. Control. Fusion* **56** 095019
- [12] Heikkinen J A and Sipilä S K 1995 Power transfer and current generation of fast ions with large- k_θ waves in tokamak plasmas *Phys. Plasmas* **2** 3724–33
- [13] Varje J, Särkimäki K, Kontula J, Ollus P, Kurki-Suonio T, Snicker A, Hirvijoki E and Äkäslompolo S 2019 High-performance orbit-following code ASCOT5 for Monte Carlo simulations in fusion plasmas (arXiv:1908.02482 [physics])
- [14] van Rij W I and Hirshman S P 1989 Variational bounds for transport coefficients in three-dimensional toroidal plasmas *Phys. Fluids B* **1** 563–9
- [15] Hakan S 2021 *NEOTRANSP* (available at: <https://gitlab.mpcdf.mpg.de/smithh/neotransp>)
- [16] Lazerson S A *et al* (the W7-X Team) 2021 Modeling and measurement of energetic particle slowing down on Wendelstein 7-X *Nucl. Fusion* **61** 096005
- [17] Lazerson S A *et al* (the W7-X Team) 2020 Validation of the BEAMS3D neutral beam deposition model on Wendelstein 7-X *Nucl. Fusion* **60** 076020
- [18] Suzuki S, Shirai T, Nemoto M, Tobita K, Kubo H, Sugie T, Sakasai A and Kusama Y 1998 Attenuation of high-energy neutral hydrogen beams in high-density plasmas *Plasma Phys. Control. Fusion* **40** 2097–111
- [19] Lazerson S A 2012 The virtual-casing principle for 3D toroidal systems *Plasma Phys. Control. Fusion* **54** 122002
- [20] Stix T H 1972 Heating of toroidal plasmas by neutral injection *Plasma Phys.* **14** 367